RESEARCH ARTICLE

Early in vivo detection of denervation-induced atrophy by luminescence transient nanothermometry

José Lifante[1,2] | Álvaro Moreno-Rupérez[3] | Erving Ximendes[2,4] |
Riccardo Marin[2,4,5] | Teresa Priego[6] | Asunción López-Calderón[3] |
Ana Isabel Martín[3] | María Paz Nieto-Bona[7] | Elena Nebot[3] |
Ginés Lifante-Pedrola[4] | Daniel Jaque[2,4,5] | Luis Monge[1,2] |
Nuria Fernández[1,2] | Miriam Granado[1,2]

[1]Facultad de Medicina, Departamento de Fisiología, Nanomaterials for Bioimaging Group (NanoBIG), Universidad Autónoma de Madrid, Madrid, Spain

[2]Nanomaterials for Bioimaging Group (NanoBIG), Instituto Ramón y Cajal de Investigación Sanitaria, Madrid, Spain

[3]Facultad de Medicina, Departamento de Fisiología, Universidad Complutense de Madrid, Madrid, Spain

[4]Departamento de Física de Materiales, Facultad de Ciencias, Nanomaterials for Bioimaging Group (NanoBIG), Universidad Autónoma de Madrid, Madrid, Spain

[5]Institute for Advanced Research in Chemical Sciences (IAdChem), Autonomous University of Madrid, Madrid, Spain

[6]Facultad de Enfermería, Fisioterapia y Podología, Departamento de Fisiología, Universidad Complutense de Madrid, Madrid, Spain

[7]Facultad de Ciencias de la Salud, Departamento de Ciencias Básicas, Universidad Rey Juan Carlos, Madrid, Spain

Correspondence
Daniel Jaque, Nanomaterials for Bioimaging Group (NanoBIG), Instituto Ramón y Cajal de Investigación Sanitaria, de Colmenar Viejo Km 9, Madrid 28034, Spain.
Email: daniel.jaque@uam.es

Abstract

Denervation induces skeletal muscle atrophy due to the loss of control and feedback with the nervous system. Unfortunately, muscle atrophy only becomes evident days after the denervation event when it could be irreversible. Alternative diagnosis tools for early detection of denervation-induced muscle atrophy are, thus, required. In this work, we demonstrate how the combination of transient thermometry, a technique already used for early diagnosis of tumors, and infrared-emitting nanothermometers makes possible the in vivo detection of the onset of muscle atrophy at short (<1 day) times after a denervation event. The physiological reasons behind these experimental results have been explored by performing three dimensional numerical simulations based on the Pennes' bioheat equation. It is concluded that the alterations in muscle thermal dynamics at the onset of muscle atrophy are consequence of the skin perfusion increment caused by the
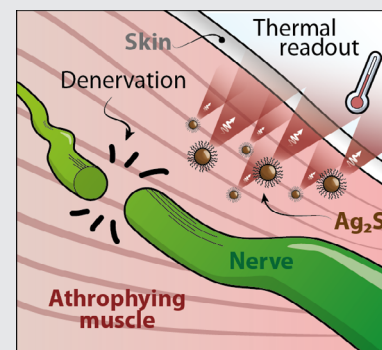
alteration of peripheral nervous autonomous system. This work demonstrates the potential of infrared luminescence thermometry for early detection of diseases of the nervous system opening the venue toward the development of new diagnosis tools.

KEYWORDS

denervation, infrared-emitting nanoparticles, luminescent nanothermometers, muscle atrophy, transient thermometry

1 | INTRODUCTION

The impact of neurological diseases in modern societies is continuously increasing due to the progressive ageing of the population. Indeed, diseases affecting the nervous system are not only a major contributor to mortality worldwide but also reduce drastically the quality of life of the affected patients [1]. One major issue regarding nervous system diseases is that they are usually associated with motor disorders that affect muscle mass producing different degrees of disability, especially those affecting the peripheral nervous system, the key regulator of muscular function [2]. A representative example is peripheral nerve damage that is associated with secondary muscle atrophy that often results in disability, such as occurs during nerve denervation, where tissue innervation is lost after section of the nerve [3–5]. Early diagnosis and the investigation of the underlying mechanisms linking denervation and atrophy become critical to minimize the social impact of denervation-induced atrophy [6].

There are two routes for the development of new diagnosis tools for denervation-induced muscle damage. One way is to develop new technologies to improve the detection of already proved biological indicators of denervation-induced muscle damage, such as muscle size or biological markers. A second approach is to develop new diagnosis tools based on the monitoring of alternative physiological parameters also altered by a denervation event. In this sense, alterations in muscle function induced by peripheral nerve injury could be associated with changes in muscle temperature due, at least in part, to alterations in mass [7], in blood flow and in muscle metabolism [8–12]. Consequently, intramuscular thermal dynamics could be potentially used as a diagnosis indicator of muscle atrophy. However, to the best of our knowledge, this fact has never been experimentally demonstrated because of lack of appropriate methods for remote intramuscular thermal reading. Minimal invasiveness is required to avoid muscle alteration and to reduce damage induced, for instance, by the implantation of a macroscopic thermal sensor [13]. At the same time, intramuscular thermal reading should be achieved in a cost-effective manner and with high temporal resolution.

These two last conditions discard other techniques capable of subtissue thermal reading such as MRI [14].

Luminescent nanothermometers (LNThs) are nanoparticles whose luminescence is strongly temperature dependent in such a way that remote and real-time thermal sensing is possible from a simple analysis of their luminescence. When the LNThs operate within the infrared biological windows (spectral regions where absorption and scattering of tissues are minimized, extending from 800 until 1500 nm), they can provide accurate thermal readouts of internal organs and tissues. Such remote thermal sensing is achieved in real time so that they make possible to access to the thermal dynamics of internal organs and tissues [15]. The development of infrared emitting LNThs has led to the appearance of a new technology denominated Transient Thermometry (TT), which has already been used for in vivo early diagnosis of tumor development and of ischemia [16, 17]. Despite all these promising results, the application of TT for early detection of denervation-induced muscle damage is still pending.

In this work, we demonstrate how infrared emitting Ag_2S LNThs can be for in vivo recording of the thermal dynamics of muscles in presence of a denervation event. In vivo experimental results demonstrate how the thermal behavior of muscles is significantly altered even at short (<1 day) times after denervation. The denervation-induced pathological alterations at the origin of the changes in muscular thermal dynamics are discussed by comparing experimental data and numerical simulations based on Penne's bioheat equation. The results included in this work reveal how TT in combination with infrared-emitting LNThs can be used for early diagnosis of denervation-induced muscle damage and future diagnosis of disorders affecting the musculoskeletal system.

2 | RESULTS AND DISCUSSION

2.1 | Characterization of Ag_2S LNThs

Ag_2S LNThs employed all along this work present a spherical geometry with an average diameter of 10 nm
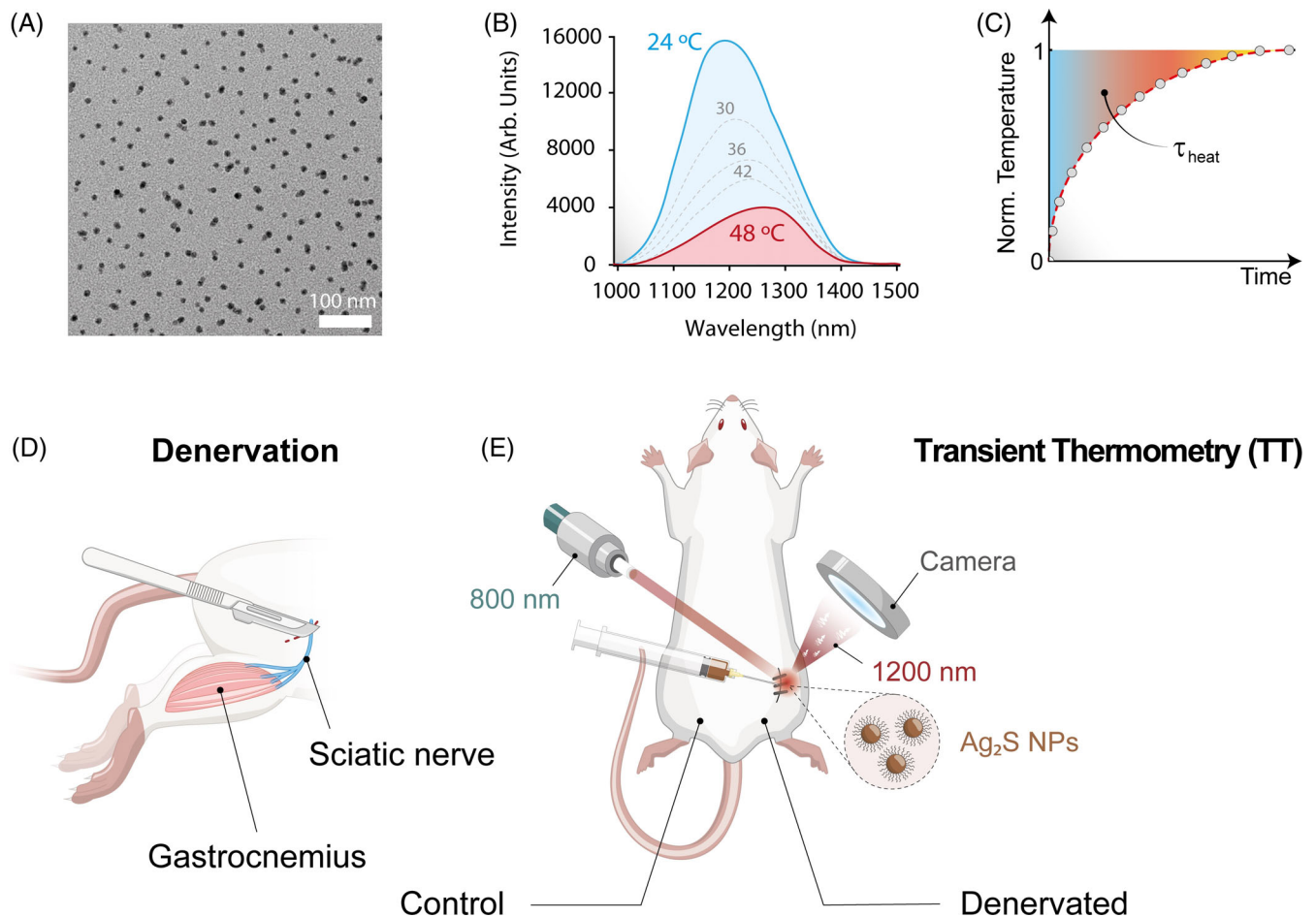
FIGURE 1 (A) TEM images of Ag$_2$S NPs from which the size distribution was estimated. (B) Thermal dependence of the luminescence generated by Ag$_2$S LNThs diluted in NaCl 0.9% saline spectra under 808 nm excitation. (C) Illustrative curve of the thermal dynamics of a tissue subjected to a heating cycle. (D) Schematic representation of denervation protocol in the rat model. (E) Experimental setup employed.

(Figure 1A). Under 800 nm optical excitation, the Ag$_2$S LNThs show a broad emission band centered at 1200 nm, whose intensity decreases monotonously with temperature within the 24–48°C range, as it has been widely reported (Figure 1B) [18]. This behavior has been associated to a temperature-induced increment in the non-radiative decays due to phonon coupling. The emitted intensity decreases linearly with temperature allowing for an unequivocal determination of temperature alterations from intensity data. Such a feature allowed to investigate the thermal dynamics of internal tissues and organs by TT (Figure 1C) [19].

2.2 | Animal model and experimental set-up for in vivo intramuscular thermal sensing

The model of peripheral sciatic nerve denervation in rat investigated in this work is depicted in Figure 1D. This model is known to alter the neuro-muscular feedback

necessary for proper muscle function [20]. A detailed description of the denervation procedure followed in this work is described with detail in Section 4. Briefly, surgery was performed on isoflurane anesthetized rats. After an incision at mid-posterolateral area of the thigh, the sciatic nerve was identified, clamped, and cut. Then, the incision was closed with surgical stitches. The same surgical procedure was performed on the left side of the lumbar spine but without cutting the nerve (control limb). After surgery, animals were allowed to recover for 24 h. If after the recovery period, no signs of infection and/or inflammation were observed, we proceeded with the thermal transient experiments (Figure 1E). In short, 24 h after denervation surgery, a dispersion of Ag$_2$S LNThs were injected into the gastrocnemius muscle in both limbs. The non denervated limb (left) was used as a SHAM control to assess the potential effects of the surgical procedure itself. The muscle under study was then illuminated with a fiber-coupled 800 nm laser. This laser played a double role: on one hand, it led to a local increment of temperature due to the light absorption of both
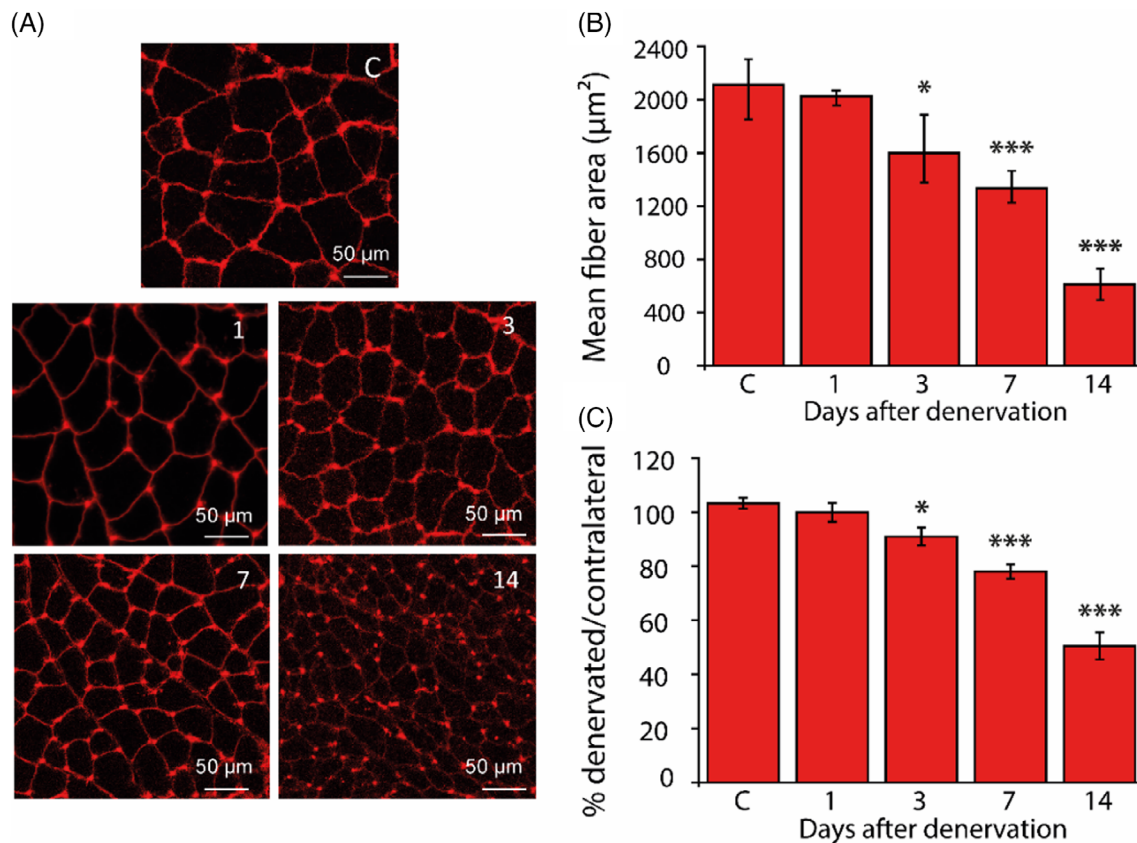
(A)

(B)

(C)

FIGURE 2   (A) Representative histological transverse sections from fast fiber region of gastrocnemius muscle stained with fluorescent wheat germ agglutinin (red). Section from control (C) rats or in rats 1, 3, 7, and 14 days post-denervation. Mean fiber area (B) and percentage of decrease of gastrocnemius muscle (C) compared to SHAM contralateral limb. Values represent the means ± SEM. One-way ANOVA was performed followed by LSD post hoc test: *$p < 0.01$, **$p < 0.001$** versus control rats.

tissues and Ag_2S LNThs and, on the other hand, it triggered the emission of infrared luminescence of Ag_2S LNThs. The infrared radiation emitted by Ag_2S LNThs was collected by an infrared objective coupled to a fluorescence camera that allowed the acquisition of fluorescence images of the investigated muscle. Analysis of fluorescence images made possible to build up intramuscular thermal videos that were used afterwards to obtain the time-evolution of muscle temperature during the heating process. An infrared thermal camera was also used to monitor the increment in the skin (surface) temperature. Special care was taken to keep the laser-induced temperature increments below 5°C to avoid any damage.

2.3 | Molecular and physiological evidences of sciatic nerve denervation

Prior to the development of the in vivo transient thermometry experiments, we conducted a battery of experiments that together gave us the picture of the dynamics underlying muscular degeneration with time. In the first set of animals ($n = 6$), we studied how the sciatic

denervation affected the gastrocnemius muscle at the molecular and histological level at different times after denervation (1, 3, 7, and 14 days post denervation). Figure 2B shows the effect of sciatic denervation on mean fiber area as measured after histological analysis (Figure 2A) and on total gastrocnemius weight (Figure 2C). As it can be observed, denervation induces gastrocnemius atrophy since both gastrocnemius weight and mean fiber area were markedly decreased, reaching on Day 14 after denervation −48% and −27% values of those of control individuals. In contrast, no significant differences exist at Day 1 post denervation in muscle.

We also evaluated the mRNA expression of well-known muscle atrophy markers that are susceptible to change after skeletal muscle denervation. The mRNA levels of the γ subunit of the nicotinic acetylcholine receptor (nAChR) were dramatically increased from Day 3 on, and this increase was significant on Days 7 and 14 post-denervation (Figure 3A, $p < 0.01$). These results are in agreement with previous studies which found that upregulation of this fetal receptor subtype is associated with hypersensitivity to the neurotransmitter ACh after muscle denervation [21]. We also analyzed the gene
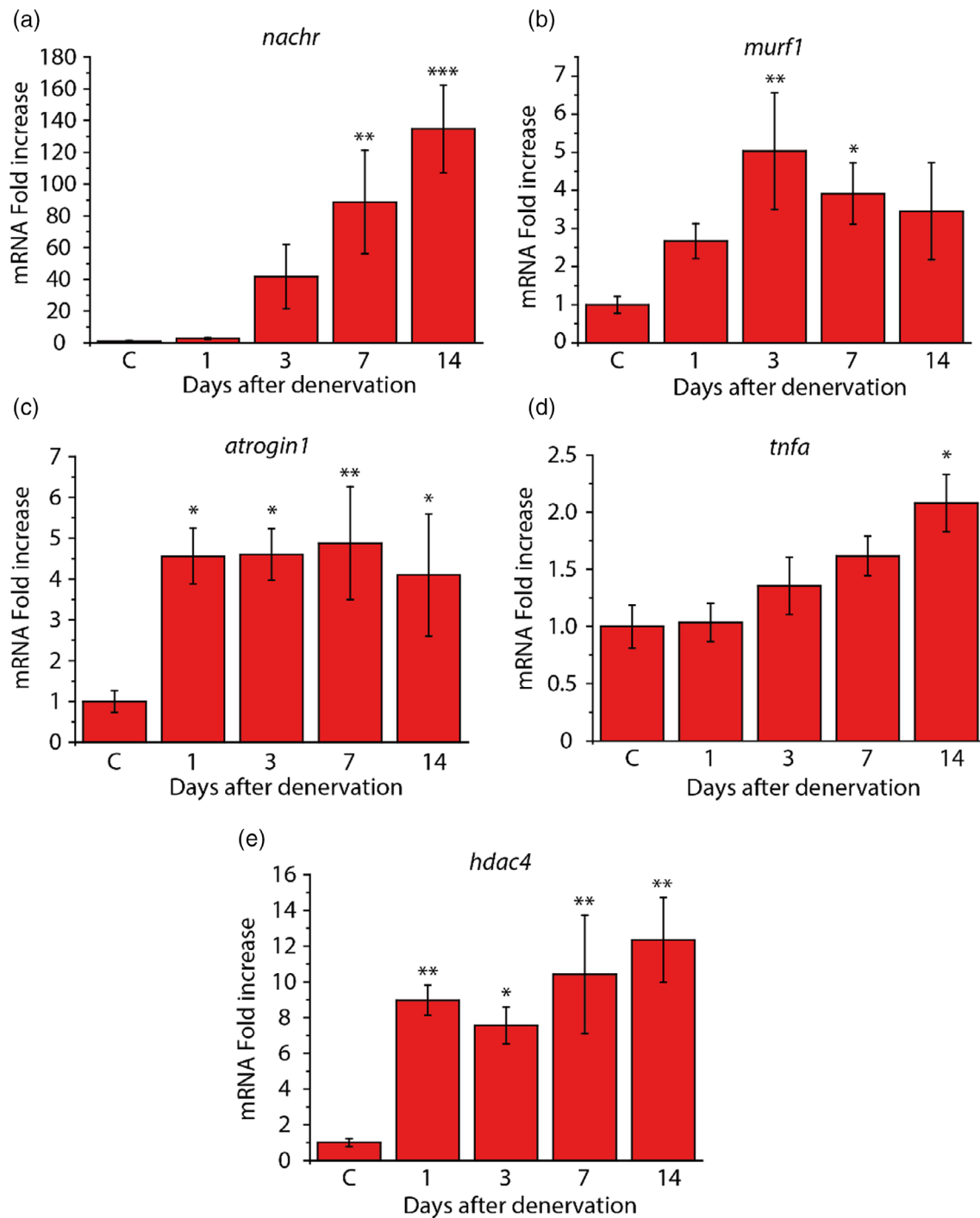
FIGURE 3 Evolution of mRNA Fold increase expression of: (A) nicotinic cholinergic receptor (nachr); (B) murf1; (C) tumor necrosis factor-α (tnfa); (D) atrogin 1; and (E) hdac4 in the gastrocnemius muscle of control and sciatic denervated animals after 1 3, 7, and 14 days post-denervation. mRNA levels were measured by real-time qPCR and expressed relative to the mean value of the control rats. Values are represented as means ± SEM. One-way ANOVA was performed followed by LSD post hoc test. $*p < 0.05$, $**p < 0.01$, $***p < 0.01$ versus control rats.

expression of muscle-specific E3 ubiquitin ligases Atrogin-1 and MuRF1, since these ligases are markers of muscle proteolysis by the ubiquitin-proteasome system, which is involved in the development of muscle atrophy induced by several conditions including denervation [22]. As shown in Figure 3B,C, there was also a significant increase in the gene expression of MuRF1 on Days 3 and 7, whereas the gene expression of Atrogin-1 was significantly elevated at all stages of the study including Day 1. The expression of the proinflammatory cytokine tumor necrosis factor-α (TNFα) showed a trend to increase in the gastrocnemius, but this increase was very slight and
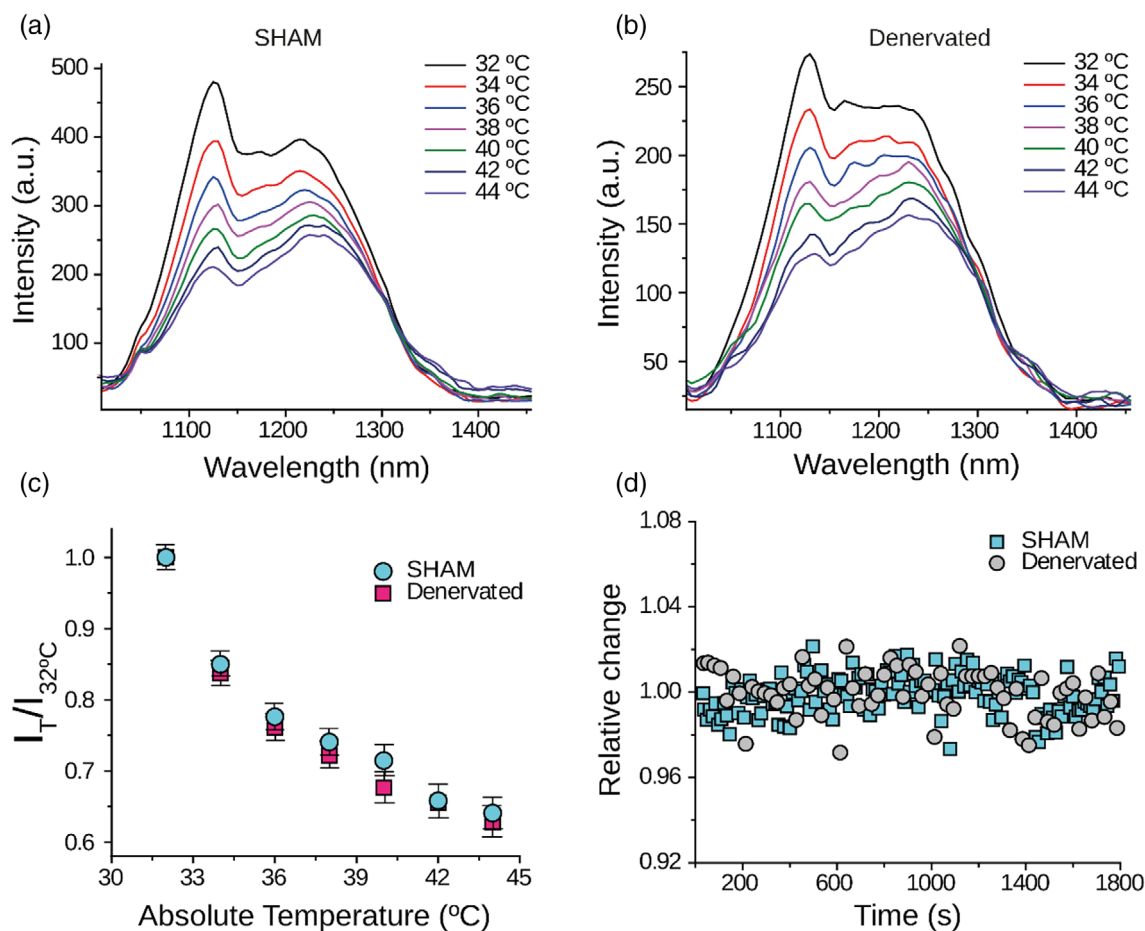
FIGURE 4 Emission spectra generated by Ag$_2$S LNThs within a control (A) and denervated (B) gastrocnemius muscle as obtained at different temperatures. Data in (A,B) were obtained in ex vivo conditions and by using a continuous wave 800 nm laser for excitation. (C) Evolution of the infrared emitted intensity generated by Ag$_2$S LNThs within a control and denervated gastrocnemius muscle as measured in ex vivo conditions. (D) Time evolution of the infrared luminescence intensity generated by Ag$_2$S LNThs within a control and denervated gastrocnemius muscle evidencing the absence of degradation. Results were obtained in in vivo conditions.

only statistically significant on Day 14 after denervation (*$p < 0.05$, Figure 3A). Finally, the mRNA levels of the histone deacetylase HDAC4 were overexpressed in gastrocnemius muscle from Day 1 to 14 (Figure 3E, **$p < 0.01$). These results agree with those reported by other authors in which HDAC4 rapidly increase in skeletal muscle upon denervation mediating the development skeletal muscle atrophy through regulation of MuRF1 and Atrogin-1 and the ubiquitin-proteasome system [23, 24].

Data included in Figures 2 and 3 evidence that our model is, indeed, causing denervation-induced atrophy. At the same time, experimental data indicate that the onset of denervation-induced atrophy is not evidenced neither by the muscle weight nor by most of the biomarkers traditionally analyzed. As a matter of fact, at Day 1 post denervation, there is not any alteration in the muscle weight and only two (*atrogin1* and *hdac4*) of the five biomarkers reveal the existence of muscle atrophy.

2.4 | In vivo transient thermometry: Experiments and simulations

In this section, we explore the potential use of TT to establish a connection between the early stages of denervation-induced muscle atrophy and alteration in muscle thermal behavior. To access the intramuscular temperature, we use the already described Ag$_2$S LNThs as luminescence-based thermal reporters, which were injected within the muscle as described in Section 2.3. We first tested their ability for intramuscular thermal sensing. To do so, we analyzed the luminescence of Ag$_2$S LNThs within health (sham) and denervated muscles (ex vivo experiments). Figure 4A shows the emission spectra corresponding to Ag$_2$S LNThs within a healthy (control) gastrocnemius muscle as a function of temperature. It is evident how the broadband emission band of Ag$_2$S LNThs is distorted by the absorption of muscular tissue. This effect, already observed in vivo in a great

variety of organs and tissues, avoids reliable absolute thermal reading based on the widely applied radiometric approach [25, 26]. Nevertheless, the luminescence intensity generated by Ag$_2$S LNThs within the gastrocnemius muscle follows a monotonous decrease with temperature (see Figure 4C) that can be used to determine intramuscular thermal variations. The emission spectra generated by the Ag$_2$S LNThs within the gastrocnemius muscle subjected to denervation are shown in Figure 4B as obtained at different temperatures. No relevant differences are found when compared with the results obtained in the control muscle; in both health and denervated muscle, we obtained the same tissue-induced perturbations and same temperature-induced luminescence quenching (Figure 4C). This indicates that potential changes induced in the muscular tissue by denervation have no effect on the luminescence properties of Ag$_2$S LNThs. The thermal quenching observed for Ag$_2$S LNThs in both control and denervated muscle makes possible monitoring relative changes in the intramuscular temperature by a straightforward analysis of the fluorescence images (simple analysis of collected intensity). Finally, we also explored the stability of our Ag$_2$S LNThs in both control and denervated muscles at the in vivo level. Both muscles were irradiated for more than 30 min and the time evolution of the fluorescence intensity was continuously recorded. Results included in Figure 4D reveals that the Ag$_2$S LNThs were stable emitting units in both control and denervated muscles. Thus, any change in the infrared fluorescence intensity observed during in vivo experiments can be directly correlated to temperature-induced changes and not to a medium-induced deterioration of the Ag$_2$S LNThs. The main advantage of using the emitted intensity as thermal reporter is that it does not require the acquisition of the emission spectra and, therefore, the use of any spectrophotometer. Instead, the thermal readout can be obtained from the analysis of the fluorescence images and, thus, only an infrared fluorescence camera is required. Of course, this experimental simplicity is gained at expenses of an readout of absolute temperature that can be obtained, for instance, by using lifetime-based thermometry.

Once the potential of our Ag$_2$S LNThs for monitoring intramuscular temperature changes was demonstrated, we proceed to evaluate in vivo intramuscular transient thermometry measurements following the experimental procedure described in Section 2.2 and in Figures 1E and 5A shows the time evolution of intramuscular temperature changes induced by a 1.5 W/cm^2 800 nm laser beam. Results obtained from both control and denervated gastrocnemius muscles in in vivo conditions were included. Relevant differences between heating dynamics of control and denervated muscles are observed, especially at long times after the start of heating process. Although the

magnitude of laser-induced heating is similar in control and denervated muscles, control muscle shows a faster heating dynamic than the denervated one. Indeed, these different heating rates lead to final temperature increments that can be different by more than 1°C after 5 min of heating. To quantify these differences, the heating curves were fitted to an exponential growth expression:

$$\Delta T = \Delta T_0 (1 - \exp(-t/\tau_h)) \tag{1}$$

where ΔT_0 is the temperature increment achieved at long times in steady state and τ_h is a characteristic heating time. Fitting of experimental data to Equation (1) has been demonstrated a valid approach for the analysis of thermal dynamics of ischemia and tumor development [16]. Figure 5B shows the average characteristic heating time of both control and denervated muscles as obtained from the experiments performed in six individuals 24 h after denervation. As it is observed, denervation leads to a significant reduction in the characteristic heating time of the gastrocnemius muscle. In previous works, changes in the characteristic heating/cooling times have been interpreted in terms of changes in the tissue perfusion, tissue mass, and thermal properties of tissues. In the case of this study, all these parameters could be changing simultaneously, and, at a first glance, it is not possible to identify the physiological cause of the reduction in τ_h caused by denervation. Numerical simulations based on the Pennes' equation of heat transport in living tissues are required to get a further insight about the physiological mechanisms at the origin of the denervation-induced changes in the thermal behavior of muscles. According to Pennes' work, the time evolution of tissue temperature (T_t) after the application of an external heat source should reveal changes in perfusion [27]:

$$\frac{\partial T_t}{\partial t} = \frac{1}{\rho c} \nabla(\kappa \nabla T_t) + \frac{\rho_b c_b}{\rho c} \omega_b (T_b - T_t) + \frac{q_m}{\rho c} + \frac{q_v}{\rho c} \tag{2}$$

where t is the time after the heating source has been switched on, ρ and ρ_c are the density of tissue and blood (in kg·m^{-3}), respectively, c and c_b are the specific heat of tissue and blood, respectively, κ is the tissue thermal conductivity (in W·m^{-1}·K^{-1}), ω_b is the blood perfusion rate (in s^{-1}), T_b is the blood temperature (in K), q_m is the metabolic heat generation (in W·m^{-3}), and q_v is the supplied external power per unit volume (in W·m^{-3}). For applying the heat diffusion equation, energy loss from the considered volume must to be taken into account. Losses from radiation are negligible (see Section S1 in Supporting Information) and are not considered in the heat balance equation. At the same time, convection is modeled according to Newton's law of cooling [28]:
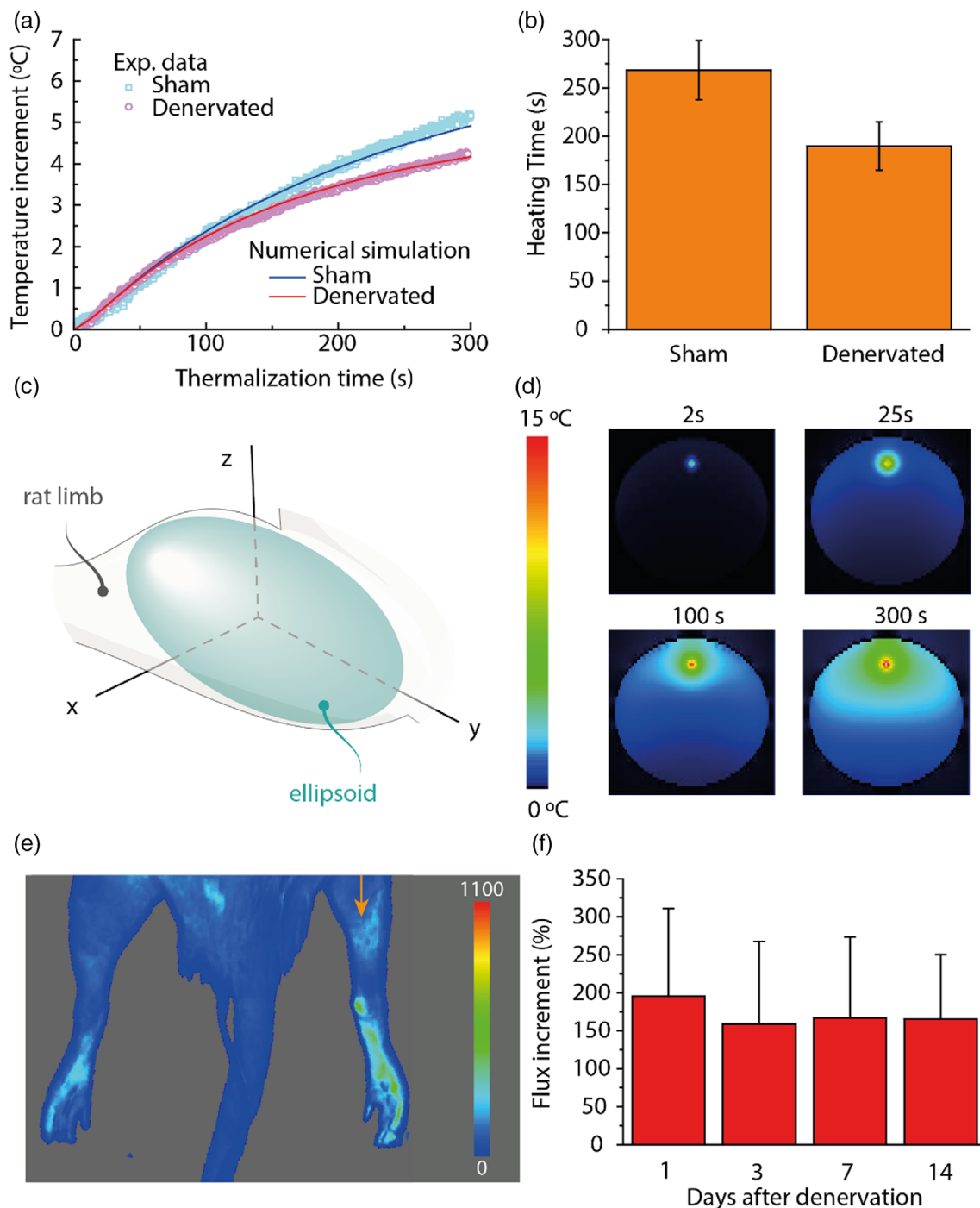
FIGURE 5 (A) In vivo time evolution of muscle temperature increments as obtained in a denervated and control gastrocnemius muscle. Dots are experimental data and solid lines are the results from three-dimensional numerical simulations provided by the bioheat equation using different perfusion rates: red line, 0.003 s^{-1}; blue line, 0.007 s^{-1}. (B) Average characteristic heating time corresponding to denervated and control gastrocnemius muscles as obtained from the fit of experimental data to Equation (1). For this experiment, $n = 3$ animals were employed. Values are represented as means ± SEM. (C) Schematic representation of the geometry assumed for the development of numerical simulation. Gastrocnemius muscle is assumed to have an ellipsoidal shape being embedded into the rat limb. (D) Simulated cross sectional thermal images of the gastrocnemius muscle during the laser heating process as obtained at different heating times. Hots spot matches the located of the Ag_2S injection. (E) Laser Speckle (skin perfusion) image of an individual subjected to the denervation surgery in its right limb (indicated by an arrow). (F) Flux increment percentage produced in the denervated limb in respect to control limb as obtained at different times after denervation. For this experiment, $n = 3$ animals were employed. Values are represented as means ± SEM.

$$q_c = h_c(T_e - T_s) \quad (3)$$

where T_e is the environment temperature, T_s is the surface temperature, and h_c is the heat transfer coefficient.

Equation (2), together with the boundary condition supplied by Equation (3), is solved by a 3D-finite difference scheme using the Douglas–Gunn method, which provides an algorithm that is second order accurate in both time and space derivatives [29]. Details about the procedure followed for numerical simulations are given in Section S1 of Supporting Information. Parameters of the model for both tissue and skin are listed in Tables S1 and S2 in Supporting Information as obtained from previous works [30]. Figure 5C shows some cross sectional thermal images corresponding to the limb as obtained at different times after switching On the heating source. The hot spot corresponds to the spatial location of the injected Ag$_2$S LNThs as they have been identified as the main heating source in our experimental conditions (see Section S2 of Supporting Information). Continuous lines in Figure 5A shows the results of the 3D numerical simulation using the laser source as the heating term q_v in the bioheat equation. The temporal evolution of the temperature increment in the control limb (red line) is well modeled using a perfusion blood rate of 0.003 s^{-1}, in both skin and inner tissue, according to reported values [31]. On the other hand, the data corresponding to the denervated limb can be well fitted by using a larger value of 0.007 s^{-1} in the superficial (skin) blood perfusion rate. Denervation could also cause alters the muscle metabolic activity and, hence, can also affect the thermal dynamics of the muscle thorough the term $\frac{q_m}{\rho c}$ in Equation (2). Nevertheless, alterations in the metabolic activity have not been considered as a possible cause of the changes in the thermal dynamics of denervated muscle: according to the data included in Table S1 of Supporting Information, $\frac{q_m}{\rho c} \ll \frac{\rho_b c_b}{\rho c} \omega_b (T_b - T_t)$ so that thermal dynamics of muscle is governed by blood perfusion. At this point, we should highlight that the numerical simulations in Figure 5A may not perfectly reflect the real conditions within tissues. We, indeed, made a simplifying assumption that the thermal properties of tissues remain constant within the temperature range we investigated ($<6°C$). This is a basic approximation, and it is possible that deviations between our numerical simulations and experimental data could arise from variations in the thermal properties of tissues within this temperature range. However, it is still worth noticing that despite these potential discrepancies, our numerical simulations effectively capture the distinctions between sham and denervated tissues.

Numerical simulations suggest that the experimental data and the differences in thermal behavior between health and denervated gastrocnemius muscles can be well explained by considering an increment in the superficial blood perfusion rate due to denervation. This would be a plausible explanation for the denervation-induced change in τ_h but it would imply that, even at short post-denervation times, skin perfusion is affected due to denervation. To verify this hypothesis, we have performed laser Speckle experiments to detect denervation-induced changes in the skin perfusion at short post-denervation times. Figure 5D shows the perfusion images of a representative rat subjected to denervation surgery on its right limb (indicated by an arrow). The perfusion image was obtained 1 day after denervation and reveals a clear increment of perfusion in the denervated limb. Indeed, we have obtained that skin perfusion has been almost doubled in the denervated limb. This experimental observation is in very good agreement with numerical simulations that concluded that the denervation-induced changes in the muscle thermal dynamics at short time post denervation could be explained by three-fold increment in the skin perfusion (from 0.003 s^{-1} up to 0.007 s^{-1}). Furthermore, measurements performed at different post-denervation times reveal that this denervation-induced increment in perfusion rate remains up to 14 days after denervation (Figure 5F, that includes the percentage of flux increment as a function of the post-denervation time as calculated from the comparison between the speckle images of healthy and denervated limbs). The denervation-induced increment in skin perfusion does not only impacts on the muscle thermal dynamics but also on the skin temperature as it has been evidenced by the infrared thermometry experiments included in Section S3 of Supporting Information. At this point, we would like to highlight that, according to Figure 5F, early diagnosis of denervation-induced atrophy could be also achieved by detecting the denervation-induced change in the superficial blood perfusion, that is by using speckle imaging instead of infrared luminescence thermometry. The advantages of infrared luminescence thermometry as a diagnosis tool would be the possibility of measuring in daylight conditions, the potential use of nanothermometers as drug carriers, and the diagnosis in tissues with different pigmentations. The potential translation of transient thermometry into the clinics is difficult as it requires long measuring times (minutes). We state here that the different heating rates can be also extracted from a proper analysis of the first seconds after the heat pulse when the temperature variation follows a quasi-linear behavior with time. Furthermore, a reduction in the measuring time would be possible by increasing the temperature relaxation rate. This, in turn, can be reached by reducing the volume of the tissue that is being subjected to the heating/cooling. These could be future steps to be taken to translate transient thermometry into the clinics.

So, we conclude that the changes taking place in the thermal dynamics of a muscle at the onset of denervation-induced atrophy are caused by the increment in the superficial (skin) blood perfusion. From a physiological point of view this, indeed, is supported by previous experimental observations. In endothermic animals such as rat and humans, internal tissues regulate their temperature through modulation of skin perfusion. This is one of the main mechanisms responsible for tissue cooling when excessive heat is perceived by internal receptors [32]. As a matter of fact, skin is enriched in pre-capillary sphincters that allow circulation of blood flow from internal organs to the skin when excessive heating is present, and vice versa. These peripheral micro vessels are innervated by sympathetic fibers from the autonomous nervous system by adrenergic receptors [33]. In contrast, the skeletal muscle microcirculatory network does not possess such capability, and its intrinsic thermal regulation relies more or local metabolic cues directly related to muscle contraction. Relevant for this study, sciatic nerve denervation induces especially relevant changes in skin perfusion, while muscle perfusion less affected through after this type of injury [34].

3 | CONCLUSIONS

In summary, we have demonstrated that is possible to evidence the onset of denervation-induced muscular atrophy at the in vivo level by nanoparticle-based transient thermometry. Infrared emitting Ag_2S LNThs have been used to monitor the thermal dynamics of gastrocnemius muscles in presence and absence of denervation. Experimental data revealed how denervation induces significant changes in the intramuscular thermal dynamics even at short (<24 h) times after denervation when atrophy has just started. At such, short post-denervation times, the onset of atrophy was not evidenced by macroscopic observations (muscle weight) and was revealed only by some of the atrophy markers so that nanoparticle-assisted transient thermometry emerges as an early diagnosis tool. Comparison between experimental data and three-dimensional numerical simulations concluded that the denervation-induced changes in intramuscular thermal dynamics are correlated with the increment in the superficial (skin) perfusion due to the alteration of peripheral nervous autonomous system.

This study does not only introduce nanoparticle-assisted transient thermometry as a tool for early diagnosis of diseases of nervous system, but it also shows the prowess of luminescence thermometry in providing novel insight into complex biological processes at the in vivo level. Combined with the powerful approach of transient thermometry

and numerical calculations exploration of further complex biological phenomena is envisaged.

In conclusion, nanoparticle-assisted transient thermometry may be a good technique to be combined with other methods such as advanced modalities of MRI for the early diagnosis of diseases and/or conditions that are associated with modifications in tissue temperature, including denervation-induced muscle atrophy.

4 | EXPERIMENTAL SECTION

4.1 | Compliance with ethical principles and relevant legislations

All procedures with animals meet with:

1. The approval by the local Ethics Committee for Animal Research at the host institution according to regional and national regulations. The investigation conforms to the Guide for the Care and Use of Laboratory Animals published by the European Parliament (EU directive 2010/63/EU).
2. The royal ordinance RD 53/2013, February 1, which establishes the basic rules applicable for the protection of animals during experimental and other scientific purposes, including teaching.
3. The order ECC/566/2015, March 20, establishes the training requisites that the personnel handling, breeding, or providing animals for experimentation or teaching has to fulfill according to the Spanish legislation.
4. The Transparency Committees of the Universidad Autónoma de Madrid (UAM), Universidad Complutense de Madrid, and the Autonomic Government of Madrid (PROEX 038.0/21) based on the statement supporting European Directive 2010/63/EU ("Directive") on the protection of animals used for scientific purposes. These Committees are created by the European institution EARA.

4.2 | Ag_2S characterization

The size and morphology of Ag_2S NPs were characterized by using a JEOL JEM1400 Flash TEM microscope. Samples were prepared by adding a sample drop on top of formvar-coated copper grids and letting them dry at room temperature.

For steady-state luminescence measurements, we used a single-mode fiber coupled laser diode operating at 808 nm as the excitation source (Lumics BTF14). The laser radiation was first collimated and then focused into a cuvette containing the aqueous dispersion of Ag_2S nanoparticles. The

luminescence emitted by the dispersion was spectrally analyzed by a fiber-coupled spectrometer (Kymera 193i, Andor) with a diffraction grating featuring 75 g/mm and blazed at 1700 nm. The emission was recorded using an InGaAs CCD camera (Andor iDus DU490A). The cuvette containing the nanoparticles was placed in a temperature-controlled compact spectrometer sample compartment (QPod 2e™ from Quantum Northwest, Inc.). This allows to change the sample temperature between 10 and 60°C with a temperature accuracy of 0.15°C.

4.3 | Rat sciatic nerve denervation model

Studies were performed on male Wistar rats (Charles River, Wilmington, MA, USA) weighing 200–250 g. They were housed under a temperature and humidity-controlled environment with a 12 h light–dark cycle and free access to food and water. Sciatic nerve denervation was performed as previously described under isoflurane anesthesia [35]. A 2-cm skin incision was made in the mid-posterolateral area of the thigh. A 10–12 mm pocket was made along the separation of the muscle groups or bundles and deepened by blunt dissection to expose the sciatic nerve. The sciatic nerve of the hind limb was then cut. For the accompanying sham operation, the sciatic nerve of the hind limb was exposed but not transected. The muscle groups were approximated and returned to close up the created pocket, and the skin incision was closed with surgical staples. In order to facilitate imaging experiments, both control and denervated limbs of rats were shaven using a rat trimmer and shaven cream, allowing to direct exposure of skin to the surface. For biochemical and histological determinations, 12 rats underwent sciatic nerve of the right hind limb, and euthanized 1, 3, 7, and 14 days afterwards. Four rats were submitted to sham surgery of both the right and the left hind limbs to serve as control group and were euthanized 7 days after surgery. The gastrocnemius muscles were removed, dissected, and rapidly frozen in liquid nitrogen and stored at −80°C until mRNA analysis.

For blood perfusion and transient thermometry experiments, we employed rats at Day 1 post denervation, as biochemical but not muscle weight changes could be detected at that time point. To do so, six rats were submitted to sciatic nerve denervation of the right hind limb. The sciatic nerve of the left hind limb was submitted to sham surgery and served as control. Rats were euthanized 1, 3, 7, and 14 days after denervation and sham surgery.

4.4 | Skeletal muscle histology

The medial part of the gastrocnemius muscles were placed on a transparency film, glued at one end to a cork with gum tragacanth (Fibraguar; Fardi, Madrid, Spain). Samples were frozen in cooled isopentane by liquid nitrogen and stored at −80°C. Cryosections of 10 μm were subjected to immunohistochemistry. The extracellular matrix was detected by Wheat Germ Agglutinin (WGA) labeled with Texas Red (W849; Invitrogen; 1 mg/mL). Sections were mounted with Prolong-Gold antifade reagent combined with DAPI (P36935, Invitrogen). Digital images from lateral area (fast fibers) were acquired and stitched into mosaic with a confocal microscope Leica SP-8. Image J software was used to measure fiber area.

4.5 | Quantitative real-time polymerase chain reaction

Total RNA was extracted from gastrocnemius muscles using TRIsure method (BIOLINE, London, UK) and cDNA was synthesized with a High Capacity cDNA Reverse Transcription Kit (Applied Biosystems, Thermo Fisher Scientific). The resulting cDNA samples were used with specific primers (Table 1) and 1 × Takara SYBR Green Premix Ex Taq (Takara BIO Inc., Otsu, Japan) to perform real time-PCR. The relative expression was calculated using the $2^{-\Delta\Delta Ct}$ method and 18S was used as a housekeeping gene.

TABLE 1 Specific primers used for quantitative real-time polymerase chain reaction.

18 S	5'-GGTGCATGGCCGTTCTTA	5'-TCGTTCGTTATCGGAATTAACC
TNFα	5'-TGAACTTCGGGGTGATCG	5'-GGGCTTGTCACTCGAGTTTT
MuRF-1	5'-TGTCTGGAGGTCGTTTCCG	5'-AAGTGATCATGGACCGGCAT
Atrogin-1	5'-GAACAGCAAAACCAAAACTCAGTA	5'-GCTCCTTAGTACTCCCTTTGTGAA
HDAC-4	5'-CACACCTCTTGGAGGGTACAA	5'-AGCCCATCAGCTGTTTTGTC
nAChR	5'-CAGAACTGCTCCCTCGTCTT	5'-TCAGCTGCAAGTTGATCTCG

4.6 | Blood flow determination (speckle)

Rats were anesthetized with a continuous flow of 1.5 iso-flurane in 100% oxygen and maintained in decubitus position with limbs fixed in extension with transparent tape. Cutaneous blood perfusion of the footpad was recorded using Laser Speckle Contrast Imaging (Moor FLPI2 system, Moor Instruments, Axminster, UK) with a laser wavelength of 785 nm. Speckle contrast, defined as the ratio of the standard deviation of pixel intensity to the mean pixel intensity, was used to measure hind limb superficial skin perfusion, because it is derived from the speckle visibility relative to the velocity of the light-scattering particles (blood). Ratio was then converted to correlation time values, which are inversely and linearly proportional to the mean blood velocity. The laser head was positioned 20 cm above the skin. After 20 min of flow stabilization, hind limb blood perfusion was measured, as described previously [36].

4.7 | In vivo transient thermometry

Once we selected the optimal power density in which we could use the maximum power without having a relevant tissue temperature increment (around $0.1°C$ after 5 min of illumination), we proceeded to perform intramuscular injections of Ag_2S nanoparticles with a concentration of 1 mg/mL. This concentration ensures a good fluorescence signal at the laser excitation densities used all along this work. Just after the injection of Ag_2S nanoparticles, isoflurane-anesthetized rats were placed in a homemade infrared in vivo imaging system. The system was equipped with a Zephir infrared camera with enhanced sensitivity in the 900–1700 nm spectral range and operating at $-70°C$ for noise and background reduction. Once placed inside the infrared imaging system, the animals were subjected to a heating process using the 800 nm laser radiation as heating stimulus. The 800 nm laser intensity was fixed to $1.5 W/cm^2$ in all the experiments. The heating laser was switched off when a superficial temperature increment of 5 degrees (from 34 to $39°C \pm 0.5°C$ of error) was achieved. The skin (superficial) temperature was monitored in real time with an infrared thermal camera (FLIR E40bx).

4.8 | Statistical analysis

Statistics were computed using the statistics program SPSS. Data are presented as mean ± SEM and differences among experimental groups were analyzed by one-way analysis of variance. Post hoc comparisons were made by using subsequent LSD multiple range tests. Statistical significance was set at $*p < 0.05$.

CONFLICT OF INTEREST STATEMENT
The authors declare no conflicts of interest.

DATA AVAILABILITY STATEMENT
The data that support the findings of this study are available from the corresponding author upon reasonable request.

ORCID
Daniel Jaque https://orcid.org/0000-0002-3225-0667

REFERENCES

[1] V. L. Feigin, T. Vos, E. Nichols, M. O. Owolabi, W. M. Carroll, M. Dichgans, G. Deuschl, P. Parmar, M. Brainin, C. Murray, *Lancet Neurol* **2020**, *19*, 255.

[2] T. M. Manini, S. L. Hong, B. C. Clark, *Curr. Opin. Clin. Nutr. Metab. Care* **2013**, *16*, 21.

[3] H. Kern, S. Boncompagni, K. Rossini, W. Mayr, G. Fanò, M. E. Zanin, M. Podhorska-Okolow, F. Protasi, U. Carraro, *J. Neuropathol. Exp. Neurol.* **2004**, *63*, 919.

[4] M. Salanova, G. Schiffl, B. Püttmann, B. G. Schoser, D. Blottner, *J. Anat.* **2008**, *212*, 306.

[5] J. E. Cunha, G. M. Barbosa, P. A. T. Castro, B. L. F. Luiz, A. C. A. Silva, T. L. Russo, F. A. Vasilceac, T. M. Cunha, F. Q. Cunha, T. F. Salvini, *Sci. Rep* **2019**, *9*, 6366.

[6] P. Hendrickse, M. Galinska, E. Hodson-Tole, H. Degens, *Exp. Gerontol.* **2018**, *106*, 159.

[7] K. A. Sarhane, B. R. Slavin, N. Hricz, H. Malapati, Y. Guo, M. Grzelak, I. A. Chang, H. Shappell, N. von Guionneau, A. L. Wong, R. Mi, A. Höke, S. H. Tuffaha, *Exp. Neurol.* **2021**, *339*, 113650.

[8] L. Larsson, H. Degens, M. Li, L. Salviati, Y. il Lee, W. Thompson, J. L. Kirkland, M. Sandri, *Physiol. Rev.* **2019**, *99*, 427.

[9] O. Hudlicka, *Muscles Ligaments Tendons J.* **2011**, *1*, 3.

[10] H. Fujino, H. Kohzuki, I. Takeda, T. Kiyooka, T. Miyasaka, S. Mohri, J. Shimizu, F. Kajiya, *J. Appl. Physiol.* **2005**, *98*, 1407.

[11] P. Wu, A. Chawla, R. Spinner, C. Yu, M. Yaszemski, A. Windebank, H. Wang, *Neural Regen. Res.* **2014**, *9*, 1796.

[12] S. L. McMillin, E. C. Stanley, L. A. Weyrauch, J. J. Brault, B. B. Kahn, C. A. Witczak, *Int. J. Mol. Sci.* **2021**, *22*, 4913.

[13] H. Degens, J. S. McPhee, *Inflammation, Advancing Age and Nutrition*, Elsevier, Amsterdam, **2014**, p. 247.

[14] K. A. Rupp, D. C. Herman, J. Hertel, S. A. Saliba, *J. Orthop. Sports Phys. Ther.* **2012**, *42*, 731.

[15] T. M. Jenkins, J. J. P. Alix, C. David, E. Pearson, D. G. Rao, N. Hoggard, E. O'Brien, K. Baster, M. Bradburn, J. Bigley, C. J. McDermott, I. D. Wilkinson, P. J. Shaw, *J. Neurol. Neurosurg. Psychiatry* **2018**, *89*, 248.

[16] E. C. Ximendes, U. Rocha, B. del Rosal, A. Vaquero, F. Sanz-Rodríguez, L. Monge, F. Ren, F. Vetrone, D. Ma, J. García-Solé, C. Jacinto, D. Jaque, N. Fernández, *Adv. Healthcare Mater.* **2017**, *6*, 1601195.

[17] H. D. A. Santos, E. C. Ximendes, M. Iglesias-de la Cruz, I. Chaves-Coira, B. del Rosal, C. Jacinto, L. Monge, I. Rubia-Rodríguez, D. Ortega, S. Mateos, J. GarcíaSolé, D. Jaque, N. Fernández, *Adv. Funct. Mater.* **2018**, *28*, 1803924.

[18] Y. Shen, J. Lifante, E. Ximendes, H. D. A. Santos, D. Ruiz, B. H. Juárez, I. Zabala Gutiérrez, V. Torres Vera, J. Rubio Retama, E. Martín Rodríguez, D. H. Ortgies, D. Jaque, A. Benayas, B. del Rosal, *Nanoscale* **2019**, *11*, 19251.

[19] J. W. Valvano, Dynamic changes in the optical and thermal properties of tissue during laser irradiation. In *Optical-thermal response of laser-irradiated tissue* (Eds: A. J. Welch, M. J. C. van Gemert), Springer, Netherlands, Dordrecht **2010**, p. 455.

[20] H. Sun, J. Liu, F. Ding, X. Wang, M. Liu, X. Gu, *J. Muscle Res. Cell Motil.* **2006**, *27*, 241.

[21] H. Cetin, D. Beeson, A. Vincent, R. Webster, *Front. Mol. Neurosci.* **2020**, *13*, 581097.

[22] J. M. Sacheck, J.-P. K. Hyatt, A. Raffaello, R. T. Jagoe, R. R. Roy, V. R. Edgerton, S. H. Lecker, A. L. Goldberg, *FASEB J. Off. Publ. Fed. Am. Soc. Exp. Biol.* **2007**, *21*, 140.

[23] W. Ma, Y. Cai, Y. Shen, X. Chen, L. Zhang, Y. Ji, Z. Chen, J. Zhu, X. Yang, H. Sun, *Front. Cell. Neurosci.* **2021**, *15*, 663384.

[24] V. Moresi, A. H. Williams, E. Meadows, J. M. Flynn, M. J. Potthoff, J. McAnally, J. M. Shelton, J. Backs, W. H. Klein, J. A. Richardson, R. Bassel-Duby, E. N. Olson, *Cell* **2010**, *143*, 35.

[25] B. del Rosal, E. Ximendes, U. Rocha, D. Jaque, *Adv. Opt. Mater.* **2017**, *5*, 1600508.

[26] Y. Shen, J. Lifante, N. Fernández, D. Jaque, E. Ximendes, *ACS Nano* **2020**, *14*, 4122.

[27] H. H. Pennes, *J. Appl. Physiol.* **1998**, *85*, 5.

[28] E. Bender, *Chem. Ing. Tech.* **1981**, *53*, 225.

[29] J. Douglas, J. E. Gunn, *Numer. Math.* **1964**, *6*, 428.

[30] R. L. Mcintosh, V. Anderson, *Biophys. Rev. Lett.* **2010**, *5*, 129.

[31] H. J. Li, X. X. Zhang, Y. F. Yi, *Int. J. Thermophys.* **2002**, *23*, 1631.

[32] C. J. Gordon, *Physiol. Behav.* **1990**, *47*, 963.

[33] S. S. Segal, *Microcirculation* **2005**, *12*, 33.

[34] J. M. González-Darder, D. Segura-Pastor, *Neurol. Res.* **1994**, *16*, 187.

[35] S. Ishiura, I. Nonaka, H. Sugita, T. Mikawa, *Exp. Neurol.* **1981**, *73*, 487.

[36] M. de la Fuente-Fernández, D. González-Hedström, S. Amor, A. Tejera-Muñoz, N. Fernández, L. Monge, P. Almodóvar, L. Andrés-Delgado, L. Santamaría, M. Prodanov, A. M. Inarejos-García, A. L. García-Villalón, M. Granado, *Antioxidants* **2020**, *9*, 339.

SUPPORTING INFORMATION

Additional supporting information can be found online in the Supporting Information section at the end of this article.